An Oceanic General Circulation Model in Pressure Coordinates

Huang Ruixin (黄瑞新)

Department of Physical Oceanography, Woods Hole Oceanographic Institution, Woods Hole, MA 02543, U.S.A.

Jin Xiangze (金向泽) and Zhang Xuehong (张学洪)

LASG, Institute of Atmospheric Physics, Chinese Academy of Sciences, Beijing 100029

ABSTRACT

A new oceanic general circulation model in pressure coordinates is formulated. Since the bottom pressure changes with time, the vertical coordinate is actually a pressure–σ coordinate. The numerical solution of the model is based on an energy–conservation scheme of finite difference. The most important new feature of the model is that it is a truly compressible ocean model and it is free of the Boussinesq approximations. Thus, the new model is quite different from many existing models in the following ways: 1) the exact form of mass conservation, 2) the in–situ instantaneous pressure and the UNESCO equation of state to calculate density, 3) the in–situ density in the momentum equations, 4) finite difference schemes that conserve the total energy.

Initial tests showed that the model code runs smoothly, and it is quite stable. The quasi–steady circulation patterns generated by the new model compare well with existing models, but the time evolution of the new model seems different from some existing models. Thus, the non–Boussinesq models may provide more accurate information for climate study and satellite observations.

Key words: Non Boussinesq, Pressure coordinates, Mase–conserving model

1. Introduction

Numerical modeling of the oceanic general circulation has come a long way, and it is now commonly accepted as a very important tool in understanding the oceanic circulation and climate. The first successful oceanic general circulation model, which is formulated in z–coordinates, was developed by Bryan (1969). Several major assumptions used in the model belong to the so–called Boussinesq approximations, which were first proposed by Boussinesq (1903) about 100 years ago. In a study of the thermally forced motion in a non–rotating system, Boussinesq argued that the density variability is generally very small and negligible, except in the buoyancy force term in the momentum equations. As a result, the mass continuity equation may be replaced by an equation of volume conservation.

Since then, Boussinesq approximations have been proven quite accurate for many applications, and these approximations are widely used in oceanic general circulation models. Many theoretical and numerical models have been developed based on the Boussinesq approximations. The theoretical reasoning of the Boussinesq approximations has been discussed in many papers, e.g., Spiegel and Veronis (1960), Mihaljan (1962), and Zeytounian (1989). However, most of these studies were focused on the scaling analysis of the non–rotating system, without paying much attention to the difference in the time evolution of the adjustment processes in a rotating stratified ocean. As will be shown in this study, rotation and

stratification in the ocean profoundly affect the adjustment processes of large—scale motion in response to thermohaline forcing anomalies.

Nevertheless, there has been concerned that the Boussinesq approximations may induce certain errors. First, replacing the mass conservation with an equivalent volume conservation can lead to faulty signals in the free surface elevation and bottom pressure. In the ocean, heating induces an upward lift of the sea surface, but it does not change the bottom pressure. On the other hand, heating a Boussinesq ocean does not directly affect the local free surface elevation, instead it induces a negative bottom pressure anomaly that can lead to a global adjustment process. As a result, the induced large—scale velocity convergence may eventually push the sea level upward. Thus, although the sea level at the site of heating may eventually rise after a time delay, the dynamic processes induced by these faulty signals in sea surface elevation and bottom pressure may be quite different from those in the oceans.

Furthermore, the Boussinesq approximations may cause faulty energy sources and energy transformation processes. Since the term representing the total derivative of density is discarded from the mass conservation equation, the direct transformation between the mechanical energy and internal energy is completely cut off during the diabatic process. Furthermore, the non—divergent approximation can lead to artificial sources of mechanical energy. For example, in the real oceans surface heating drives up the sea surface and thereby increases the gravitational potential energy. However, in a Boussinesq ocean volume is conserved, so heating leads to a decline in mass and the gravitational potential energy. Thus, it is clear that the application of the Boussinesq approximations violates the energy conservation law, although the influence of such approximations on the simulation of the ocean circulation remains unclear.

Up to now, many studies have been carried out on the evaluation of the difference between the Boussinesq models and non—Boussinesq models in the simulation of sea level changes (Greatbatch, 1994; Mellor and Ezer, 1995; Dukowicz, 1997). They all came to a similar conclusion that the difference in sea level changes is rather small between the Boussinesq models (assuming a global correction term to compensate the loss of mass) and the non—Boussinesq models, although there are small differences for some locations within the global domain (Dukowicz, 1997).

Since the Boussinesq approximations, in particular the non—divergent assumption, have inherent defects, we believe that a truly compressible ocean model may behave differently from the Boussinesq ocean model. In order to find the answer to this question, we have developed a Pressure Coordinates Ocean Model (PCOM hereafter). The advantage of pressure coordinates is that the continuity equation has a rather simple form in this coordinate system, so the numerical treatment in this coordinate system is relatively simple. In fact, pressure coordinates have been widely used in the study of the atmospheric circulation. Since the bottom pressure changes with time, the vertical coordinate is actually a pressure—σ coordinate.

Our model treats seawater as a fully compressible fluid. The calculation of density is based on the exact equation of state, as defined by UNESCO, and the time—dependent dynamic effects of pressure on density are included in the model. Dewar et al. (1998) showed that if the equivalent time—independent pressure is used in the density calculation, notable errors may be introduced. For example, it can introduce an error of 3Sv in the vertically integrated mass flux in the Gulf Stream recirculation region. This means that the effect of pressure variability on the density calculation cannot be neglected. In addition, the horizontal momentum equations in PCOM are exact, without using the approximation of replacing the

density with the mean density. So the model will be capable of simulating the meso—scale eddies more accurately.

Since the model is based on the exact form of mass conservation (actually the continuity equation is converted to the so—called bottom pressure tendency equation), total energy is conserved in the model. More importantly, the model eliminates the faulty source / sink of mass existing in the Boussinesq models due to surface thermohaline forcing or internal mixing. (The faulty source / sink of mass will give rise to a distorted pressure gradient force, thus, it may finally distort the adjustment processes in the model oceans). Since the new model follows circulation physics more faithfully than many existing models, we expect that the new model can simulate the time evolution of the adjustment processes more accurately.

Furthermore, since bottom pressure is a prognostic variable, the bottom pressure data obtained from the new high accuracy gravity satellite mission can be assimilated into the model, thus substantially improving the model's ability to simulate the oceanic circulation. On the other hand, although bottom pressure can be diagnosed in the Boussinesq models, their dynamic interpretation is unclear because the sign and the time evolution of the bottom pressure from such models are distorted, primarily due to the faulty source of mass.

The paper is organized as follows: The basic equations and the boundary conditions in PCOM are discussed in Section 2. The finite—difference and time splitting integration scheme are discussed in Section 3. In Section 4 the model is tested for the case of purely haline forcing in order to check the stability of the model code in dealing with the freshwater flux entering the ocean from above, and the ability of the model to adapt the natural boundary condition for salinity. The comparison of PCOM with an equivalent Boussinesq model in the simulation of the quasi—equilibrium state under wind stress and thermohaline forcing is discussed in Section 5. In addition, we will discuss the differences in the time evolution between these two models under anomalous thermal forcing. Section 6 provides the conclusion.

2. Model formulation

2.1 *The basic equations*

The horizontal momentum equations in spherical coordinates are

$$\frac{du}{dt} = f^* v - \frac{1}{a\rho\cos\theta}\frac{\partial p}{\partial \lambda} + D_u \ , \tag{1}$$

$$\frac{dv}{dt} = - f^* u - \frac{1}{a\rho}\frac{\partial p}{\partial \theta} + D_v \ , \tag{2}$$

where

$$\frac{d}{dt} = \frac{\partial}{\partial t} + \frac{u}{a\cos\theta}\frac{\partial}{\partial \lambda} + \frac{v}{a}\frac{\partial}{\partial \theta} + w\frac{\partial}{\partial z} \ , \tag{3}$$

a is the radius of the Earth, θ is the latitude, λ is the longitude, u and v are the zonal and meridional velocity components, $f^* = 2\Omega\sin\theta + \frac{u\tan\theta}{a}$ is the apparent Coriolis parameter, ρ is density, p is pressure, D_u and D_v are the frictional forces per unit mass. For large—scale motions, the vertical momentum equation is reduced to the hydrostatic relation

$$\frac{\partial p}{\partial z} = - \rho g \ . \tag{4}$$

The mass conservation equation is

$$\frac{1}{\rho}\frac{d\rho}{dt} + \frac{1}{a\cos\theta}\left(\frac{\partial u}{\partial\lambda} + \frac{\partial v\cos\theta}{\partial\theta}\right) + \frac{\partial\omega}{\partial z} = 0 \ , \tag{5}$$

where $\omega \equiv \dfrac{dz}{dt}$ is the vertical velocity.

The equation of state of sea water is

$$\rho = \rho(T,S,p) \ , \tag{6}$$

where T is potential temperature, S is salinity. In this model we use the UNESCO (1981) equation of state, modified by Jackett and McDougall (1995), using potential temperature as an independent variable. Note that during reversible adiabatic processes both potential temperature and salinity remain constant, so density changes are due to pressure changes and mixing. The tracer conservation equations are

$$\frac{dT}{dt} = \mathscr{C}_T \ , \tag{7}$$

$$\frac{dS}{dt} = \mathscr{C}_S \ , \tag{8}$$

where $\mathscr{C}_T$ and $\mathscr{C}_S$ represent the sub–grid mixing parameterization terms.

2.2 The pressure–σ coordinates

Our model is formulated using pressure as the vertical coordinate. Since bottom pressure varies with time and space, the normalized pressure–σ coordinates have therefore been adopted in this model, which is defined as

$$\sigma = \frac{p - p_t}{p_{bt}} \ , \quad p_{bt} = p_b - p_t \ , \tag{9}$$

where p_b is the bottom pressure and $p_t = p_t(\lambda,\theta,t)$ the atmospheric pressure specified at the sea surface; $\sigma = 0$ at the sea surface and $\sigma = 1$ at the bottom. The prognostic equations in the pressure–σ coordinates are

$$\frac{du}{dt} = f^* v - \frac{1}{a\cos\theta}\left(\frac{\partial\Phi}{\partial\lambda} + \frac{1}{\rho}\frac{\partial p}{\partial\lambda}\right) + D_u \ , \tag{10}$$

$$\frac{dv}{dt} = -f^* u - \frac{1}{a}\left(\frac{\partial\Phi}{\partial\theta} + \frac{1}{\rho}\frac{\partial p}{\partial\theta}\right) + D_v \ , \tag{11}$$

$$\frac{\partial p_{bt}}{\partial t} + \mathscr{L}(p_{bt}) = 0 \ , \tag{12}$$

$$\frac{\partial p_{bt}T}{\partial t} + \mathscr{L}(p_{bt}T) = p_{bt}\mathscr{C}_T \ , \tag{13}$$

$$\frac{\partial p_{bt}S}{\partial t} + \mathscr{L}(p_{bt}S) = p_{bt}\mathscr{C}_S \ , \tag{14}$$

where

$$\frac{d}{dt} = \frac{\partial}{\partial t} + \frac{u}{a\cos\theta}\frac{\partial}{\partial\lambda} + \frac{v}{a}\frac{\partial}{\partial\theta} + \dot{\sigma}\frac{\partial}{\partial\sigma} \ , \tag{15}$$

$$\mathcal{L}(\mu) = \frac{1}{a\cos\theta}\left(\frac{\partial\mu u}{\partial\lambda} + \frac{\partial\mu v\cos\theta}{\partial\theta}\right) + \frac{\partial\mu\dot{\sigma}}{\partial\sigma} \ , \tag{16}$$

$\dot{\sigma}$ is the virtual vertical velocity, $\phi = gz$ the geopotential height. Eq.12 is the bottom pressure tendency equation, which is actually the continuity equation in pressure–σ coordinates. Note that the tracer equations have been rewritten in the flux form with the aid of the continuity equation, so the prognostic variables are $p_{bt}T$ and $p_{bt}S$ rather than T and S in order to keep the total tracers conserved in the numerical model.

The diagnostic equations for $\dot{\sigma}$ and ϕ are

$$\phi = gz_b + \int_\sigma^1 \frac{p_{bt}}{\rho}\,d\sigma \ , \tag{17}$$

$$p_{bt}\dot{\sigma} = (p_{bt}\dot{\sigma})_{\sigma=0} - \sigma\frac{\partial p_{bt}}{\partial t} - \frac{1}{a\cos\theta}\int_0^\sigma \left(\frac{\partial p_{bt}u}{\partial\lambda} + \frac{\partial p_{bt}v\cos\theta}{\partial\theta}\right)d\sigma \ . \tag{18}$$

The equation of state is the same as Eq.6.

The viscous terms and the diffusion terms in the current version of our model are parameterized in terms

$$\begin{aligned} D_u = \frac{1}{p_{bt}}\nabla_\sigma \cdot (p_{bt}A_h\nabla_\sigma u) + \frac{1}{p_{bt}}\frac{\partial}{\partial\sigma}\left(\frac{\rho^2 g^2}{p_{bt}}A_v\frac{\partial u}{\partial\sigma}\right) \\ + A_h\left(\frac{1-\tan^2\theta}{a^2}u - \frac{2\tan\theta}{a^2\cos\theta}\frac{\partial v}{\partial\lambda}\right) \ , \end{aligned} \tag{19}$$

$$\begin{aligned} D_v = \frac{1}{p_{bt}}\nabla_\sigma \cdot (p_{bt}A_h\nabla_\sigma v) + \frac{1}{p_{bt}}\frac{\partial}{\partial\sigma}\left(\frac{\rho^2 g^2}{p_{bt}}A_v\frac{\partial v}{\partial\sigma}\right) \\ + A_h\left(\frac{1-\tan^2\theta}{a^2}v + \frac{2\tan\theta}{a^2\cos\theta}\frac{\partial u}{\partial\lambda}\right) \ , \end{aligned} \tag{20}$$

$$\mathcal{Q}_T = \frac{1}{p_{bt}}\nabla_\sigma \cdot (p_{bt}\kappa_h\nabla_\sigma T) + \frac{1}{p_{bt}}\frac{\partial}{\partial\sigma}\left(\frac{\rho^2 g^2}{p_{bt}}\kappa_v\frac{\partial T}{\partial\sigma}\right) \ , \tag{21}$$

$$\mathcal{Q}_S = \frac{1}{p_{bt}}\nabla_\sigma \cdot (p_{bt}\kappa_h\nabla_\sigma S) + \frac{1}{p_{bt}}\frac{\partial}{\partial\sigma}\left(\frac{\rho^2 g^2}{p_{bt}}\kappa_v\frac{\partial S}{\partial\sigma}\right) \ , \tag{22}$$

where

$$\nabla_\sigma \cdot (p_{bt}\kappa\nabla_\sigma\mu) = \frac{1}{a^2\cos^2\theta}\frac{\partial}{\partial\lambda}p_{bt}\kappa\frac{\partial\mu}{\partial\lambda} + \frac{1}{a^2\cos\theta}\frac{\partial}{\partial\theta}p_{bt}\kappa\cos\theta\frac{\partial\mu}{\partial\theta} \ , \tag{23}$$

in which A_h and A_v represent the lateral and vertical viscosity, κ_h and κ_v represent the lateral and vertical diffusivity, respectively. Here we assume that lateral mixing of a tracer is along the pressure–σ surface. In the next step, we will replace this simple parameterization by mixing tensors rotated to the local isopycnal coordinates, so that the mixing in the model will more closely follow what happens in the oceans.

In order to form a set of finite difference schemes that conserve the total energy (Zeng

and Zhang, 1987), we introduce a "pressure weighted" horizontal velocity $\mathbf{V}$

$$\mathbf{V} = (U, V) = (\sqrt{p_{bt}}\, u, \sqrt{p_{bt}}\, v) \ . \tag{24}$$

Note that $\frac{1}{2}\mathbf{V} \cdot \mathbf{V}$ represents the kinetic energy per unit volume in the pressure—σ coordinates. Multiplying by $\sqrt{p_{bt}}$ and with the aid of the continuity equation, the momentum equations are reduced to

$$\frac{\partial U}{\partial t} + M(U) = f^* V - \frac{\sqrt{p_{bt}}}{a\cos\theta}\left(\frac{\partial \phi}{\partial \lambda} + \frac{1}{\rho}\frac{\partial p}{\partial \lambda}\right) + \sqrt{p_{bt}}\, D_u \ , \tag{25}$$

$$\frac{\partial V}{\partial t} + M(V) = -f^* U - \frac{\sqrt{p_{bt}}}{a}\left(\frac{\partial \phi}{\partial \theta} + \frac{1}{\rho}\frac{\partial p}{\partial \theta}\right) + \sqrt{p_{bt}}\, D_v \ , \tag{26}$$

where M is an advection operator

$$M(u) = \frac{1}{a\cos\theta}\left(\frac{\partial u\mu}{\partial \lambda} - \frac{\mu}{2}\frac{\partial u}{\partial \lambda} + \frac{\partial v\cos\theta\mu}{\partial \theta} - \frac{\mu}{2}\frac{\partial v\cos\theta}{\partial \theta}\right) + \left(\frac{\partial \dot{\sigma}\mu}{\partial \sigma} - \frac{\mu}{2}\frac{\partial \dot{\sigma}}{\partial \sigma}\right) \ . \tag{27}$$

2.3 The boundary conditions

At all side walls and the bottom, velocity is zero and there is no heat nor salt flux across the bottom or the lateral boundaries. At the sea surface, ($\sigma = 0$) the kinematic boundary conditions are

$$p_{bt}\dot{\sigma} = -\rho_{\mathrm{f}} g F_{\mathrm{E-P}} \ , \tag{28}$$

$$\frac{\rho^2 g}{p_{bt}} A_v \frac{\partial u}{\partial \sigma} = -\tau_\lambda \ , \tag{29}$$

$$\frac{\rho^2 g}{p_{bt}} A_v \frac{\partial v}{\partial \sigma} = -\tau_\theta \ , \tag{30}$$

where $F_{\mathrm{E-P}}$ is the rate of evaporation minus precipitation; ρ_{f} is the density of fresh water; τ_λ and τ_θ represent the zonal and meridional components of the wind stress. Note that the river runoff can be combined with evaporation minus precipitation.

The turbulent mixing for temperature at the sea surface is

$$\frac{\rho^2 g}{p_{bt}} \kappa_v \frac{\partial T}{\partial \sigma} = -\frac{F_{\mathrm{h}}}{C_p} \ , \tag{31}$$

where F_{h} is the air—sea heat flux, C_p is the heat capacity of sea water.

The natural boundary condition for salinity (Huang, 1993) in the pressure—σ coordinates is a combination of the kinematic boundary condition (28) for the continuity equation and a flux condition for the salinity balance

$$\frac{\rho^2 g}{p_{bt}} \kappa_v \frac{\partial S}{\partial \sigma} = -S_1 \rho_{\mathrm{f}} F_{\mathrm{E-P}} \ , \tag{32}$$

where S_1 is the salinity of the top layer. Note that the turbulent salt flux below the sea surface exactly balances the vertical salt advection induced by evaporation minus precipitation, so

that the total salt flux across the air—sea interface is zero. The freshwater flux due to precipitation enters the ocean through the specification of the kinematic boundary condition (28), and it leads to a dilution of salinity in the ocean.

3. The finite—difference schemes

3.1 *The spatial finite—difference schemes*

The grid system is a rectangular Arakawa staggered B—grid (e.g., Bryan, 1969) containing T cells and U cells. The T cells are arranged at the integer grids where tracer quantities are defined, and the U cells are arranged at the half—integer grids where the horizontal velocity components are defined. The vertical velocity $\dot{\sigma}$ is defined on the interfaces of the T cells (i.e., at levels $\sigma_{k-1/2}$), and the geopotential height ϕ is defined at the middle level of the T cells (i.e., at levels σ_k).

The numerical model is based on the energy—conserving finite—difference schemes by Zeng and Zhang (1987). Accordingly, we introduce the following notations for average and difference at the half—integer grids and integer grids

$$(F_r)_{l+1/2} = F_{l+1} - F_l \ , \tag{33}$$

$$(\overline{F}^r)_{l+1/2} = \frac{1}{2}(F_{l+1} + F_l) \ , \tag{34}$$

$$(\delta_r F)_l = F_{l+1/2} - F_{l-1/2} \ , \tag{35}$$

$$(\overline{F}^r)_l = \frac{1}{2}(F_{l+1/2} + F_{l-1/2}) \ , \tag{36}$$

as well as at the half—integer levels and integer levels

$$(F_\sigma)_{k+1/2} = F_{k+1} - F_k \ , \tag{37}$$

$$(\overline{F}^\sigma)_{k+1/2} = \frac{1}{2}(F_{k+1} + F_k) \ , \tag{38}$$

$$(\delta_\sigma F)_k = F_{k+1/2} - F_{k-1/2} \ , \tag{39}$$

$$(\overline{F}^\sigma)_k = \frac{1}{2}(F_{k+1/2} + F_{k-1/2}) \ , \tag{40}$$

Integrating vertically, the surface pressure tendency equation may be rewritten as

$$\left[\frac{\partial p_{bt}}{\partial t}\right]_{i,j} = -\frac{1}{a\cos\theta_j}\left[\frac{1}{\Delta\lambda}\delta_\lambda \overline{PU_B}^\theta + \frac{1}{\Delta\theta}\delta_\theta \overline{PV_B\cos\theta}^\lambda\right] - \rho_f g F_{E-P} \ , \tag{41}$$

where $P = \sqrt{\overline{p_{bt}}}^{\lambda,\theta}$, $U_B = \int_0^1 U d\sigma$, $V_B = \int_0^1 V d\sigma$, $\Delta\lambda$ and $\Delta\theta$ are the zonal and meridional resolution respectively. This scheme guarantees total mass conservation, if there is no net freshwater flux across the air—sea interface over the whole model domain.

The diagnostic vertical velocity is

$$[p_{bt}\dot{\sigma}]_{i,j,k} = -\left[\rho_0 g F_{E-P} + \sigma_k \frac{\partial p_{bt}}{\partial t} + \frac{1}{a\cos\theta_j}\sum_{k=0}^{k}\left(\frac{1}{\Delta\lambda}\delta_\lambda\overline{PU}^\theta + \frac{1}{\Delta\theta}\delta_\theta\overline{PV\cos\theta}^\lambda\right)\delta\sigma_k\right],\tag{42}$$

where $\delta\sigma_k = \sigma_{k+1/2} - \sigma_{k-1/2}$ is the vertical resolution at the k-th layer.

The momentum equations may be expressed by

$$\left[\frac{\partial U}{\partial t}\right]_{i+1/2,\,j+1/2,\,k} = [-M(U) + f^* V + \pi_\lambda^{(1)} + \pi_\lambda^{(2)} + PD_u],\tag{43}$$

$$\left[\frac{\partial V}{\partial t}\right]_{i+1/2,\,j+1/2,\,k} = [-M(V) - f^* U + \pi_\theta^{(1)} + \pi_\theta^{(2)} + PD_v],\tag{44}$$

where the finite-difference scheme of the advection operator is

$$M(\mu) = \sum_{n=1}^{3}\mathcal{L}_n(\mu),\tag{45}$$

$$[\mathcal{L}_1(\mu)]_{i+1/2,\,j+1/2,\,k} = \frac{1}{2a\cos\theta_{j+1/2}\Delta\lambda}[2(\overline{u}^\lambda\overline{\mu}^\lambda)_\lambda - \mu\overline{u}_\lambda^\lambda],\tag{46}$$

$$[\mathcal{L}_2(\mu)]_{i+1/2,\,j+1/2,\,k} = \frac{1}{2a\cos\theta_{j+1/2}\Delta\theta}[2(\overline{v\cos\theta}^\theta\overline{\mu}^\theta)_\theta - \mu\overline{v\cos\theta}_\theta^\theta],\tag{47}$$

$$[\mathcal{L}_3(\mu)]_{i+1/2,\,j+1/2,\,k} = \frac{1}{2\delta\sigma_k}[2\delta_\sigma(\overline{\dot{\sigma}}^\lambda,^\theta\overline{\mu}^\sigma) - \mu\delta_\sigma\overline{\dot{\sigma}}^\lambda,^\theta],\tag{48}$$

where $u = U/P$, $v = V/P$. Note that U, V are the prognostic variables and the real velocities u and v are diagnostic variables.

The pressure gradient terms in the monentum equations are

$$[\pi_\lambda^{(1)}]_{i+1/2,j+1/2,k} = \frac{-1}{a\cos\theta_{j+1/2}\Delta\lambda}[P\overline{\phi}_\lambda^\theta],\tag{49}$$

$$[\pi_\theta^{(1)}]_{i+1/2,j+1/2,k} = \frac{-1}{a\Delta\theta}[P\overline{\phi}_\theta^\lambda],\tag{50}$$

$$[\pi_\lambda^{(2)}]_{i+1/2,j+1/2,k} = \frac{-1}{a\cos\theta_{j+1/2}\Delta\lambda}[P\overline{\overline{\alpha}^\lambda p_\lambda}^\theta],\tag{51}$$

$$[\pi_\theta^{(2)}]_{i+1/2,j+1/2,k} = \frac{-1}{a\Delta\theta}[P\overline{\overline{\alpha}^\theta p_\theta}^\lambda],\tag{52}$$

where $\alpha = \rho^{-1}$. The viscous terms are

$$PD_u = \frac{1}{Pa^2\cos^2\theta_{j+1/2}}\left[\frac{1}{\Delta\lambda^2}(p_{bt}A_h\delta_\lambda u)_\lambda + \frac{1}{\Delta\theta^2}\cos\theta_{j+1/2}(p_{bt}A_h\delta_\theta u)_\theta\right]$$
$$+ \frac{1}{\delta\sigma_k}\delta_\sigma\left(\frac{\rho^2 g^2}{p_{bt}}A_v\frac{U_\sigma}{\Delta\sigma}\right)_k$$

$$+ A_h \left(\frac{1- \tan^2\theta_{j+1/2}}{a^2} U - P\frac{2\tan\theta_{j+1/2}}{a^2\cos\theta_{j+1/2}\Delta\lambda} \overline{v}_\lambda^\lambda \right) , \tag{53}$$

$$PD_v = \frac{1}{Pa^2\cos^2\theta_{j+1/2}} \left[\frac{1}{\Delta\lambda^2} (p_{bt} A_h \delta_\lambda v)_\lambda + \frac{1}{\Delta\theta^2} \cos\theta_{j+1/2} (p_{bt} A_h \delta_\theta v)_\theta \right]$$

$$+ \frac{1}{\delta\sigma_k} \delta_\sigma \left(\frac{\rho^2 g^2}{p_{bt}} A_v \frac{V_\sigma}{\Delta\sigma} \right)_k$$

$$+ A_h \left(\frac{1- \tan^2\theta_{j+1/2}}{a^2} V + P\frac{2\tan\theta_{j+1/2}}{a^2\cos\theta_{j+1/2}\Delta\lambda} \overline{u}_\lambda^\lambda \right) . \tag{54}$$

The tracer equations are

$$\left[\frac{\partial p_{bt} T}{\partial t} \right]_{i,j,k} = - ADV(T) + DIF(T) , \tag{55}$$

$$\left[\frac{\partial p_{bt} S}{\partial t} \right]_{i,j,k} = - ADV(S) + DIF(S) , \tag{56}$$

where

$$ADV(\mu) = \frac{1}{a\cos\theta_j} \left[\frac{1}{\Delta\lambda} \delta_\lambda (\overline{PU}^\theta \; \overline{\mu}^\lambda) + \frac{1}{\Delta\theta} \delta_\theta (\overline{PV\cos\theta}^\lambda \; \overline{\mu}^\theta) \right]$$

$$+ \frac{1}{\delta\sigma_k} \delta_\sigma (p_{bt} \dot\sigma \overline{\mu}^\sigma)_k , \tag{57}$$

$$DIF(\mu) = \frac{1}{a^2\cos^2\theta_j} \left[\frac{1}{\Delta\lambda^2} \delta_\lambda (p_{bt} \kappa_h \mu_\lambda) + \frac{\cos\theta_j}{\Delta\theta^2} \delta_\theta (p_{bt} \kappa_h \cos\theta_j \mu_\theta) \right]$$

$$+ \frac{1}{\delta\sigma_k} \delta_\sigma \left(\frac{\rho^2 g^2}{p_{bt}} \kappa_v \frac{\mu_\sigma}{\Delta\sigma} \right)_k . \tag{58}$$

It is easy to prove that total salinity is conserved in this model. On the other hand, total potential temperature can be conserved if there is no net heat flux across the sea surface.

Furthermore, it can be shown that if all the variables are defined at the same time level and the frictional terms are neglected, the finite–difference equations discussed above can guarantee an accurate conversion between the mechanical energy and internal energy.

3.2 *Time–splitting integration method*

Since the model includes an explicit free surface, we therefore choose to solve the full equations by means of a time–splitting integration method (Zeng and Zhang, 1982) to over-come the time step limit imposed by the gravity wave processes. In other words, we will use a short time step to integrate the geostrophic adjustment processes (Mode–I), while using a longer time step for the advection and dissipation processes (Mode–II), and an even more longer time step for the thermodynamic processes (Mode–III).

(1) Mode–I: geostrophic adjustment process. This mode applies to the bottom pressure tendency equation, the momentum derivative associated with the pressure gradient and Coriolis terms. Potential temperature and salinity are kept unchanged during this phase of in-tegration. Thus, the prognostic equations of Mode–I may be written as

$$[p_{bt}]^{n_b+1} = \overline{[p_{bt}]}^{n_b-1} + 2\Delta t_b \left[-\frac{1}{a\cos\theta}\left(\frac{\partial\sqrt{p_{bt}}\,U_b}{\partial\lambda} + \frac{\partial\sqrt{p_{bt}}\,V_b\cos\theta}{\partial\theta}\right)\right]^{n_b} - \rho_f g F_{E-P} \ , \tag{59}$$

$$[U]^{n_b+1} = \overline{[U]}^{n_b-1} + 2\Delta t_b \left\{ f^* \frac{[V]^{n_b+1} + \overline{[V]}^{n_b-1}}{2} - \left[\frac{\sqrt{p_{bt}}}{a\cos\theta}\left(\frac{\partial\phi}{\partial\lambda} + \frac{1}{\rho}\frac{\partial p}{\partial\lambda}\right)\right]^{n_b} \right\} \ , \tag{60}$$

$$[V]^{n_b+1} = \overline{[V]}^{n_b-1} + 2\Delta t_b \left\{ -f^* \frac{[U]^{n_b+1} + \overline{[U]}^{n_b-1}}{2} - \left[\frac{\sqrt{p_{bt}}}{a}\left(\frac{\partial\phi}{\partial\theta} + \frac{1}{\rho}\frac{\partial p}{\partial\theta}\right)\right]^{n_b} \right\} \ , \tag{61}$$

where the superscript n_b denotes the n-th time level of Mode–I; Δt_b is the time step; the overbar represents a temporal filter (Asselin, 1972) that is used to remove the computational mode associated with the standard leapfrog scheme; U_b and V_b are the vertical integrals of U and V. Here a semi–implicit scheme is adopted to deal with the Coriolis terms.

The diagnostic equations are

$$[\rho]^{n_b} = [\rho(T,S,p)]^{n_t} + \left[\frac{\partial\rho}{\partial p}\right]^{n_b} ([p]^{n_b} - [p]^{n_t}) \ , \tag{62}$$

$$[\phi]^{n_b} = gz_b + \int_0^1 \left[\frac{p_{bt}}{\rho}\right]^{n_b} d\sigma \ , \tag{63}$$

where n_t represents the current time level of Mode–III. Instead of using the standard equation of state, here the density is calculated using a modified equation of state, where the density is calculated as a linear perturbation to that calculated in n_t time levels. This is a technique to reduce the computation time required for a standard density calculation. In addition, both potential temperature and salinity are held unchanged during the integration.

The integrations of Mode–I and Mode–II are synchronous. For example, when Mode–II is integrated from the $(n_c - 1)\Delta t_c$ time level to the $(n_c + 1)\Delta t_c$ time level on a normal leapfrog time step, Mode–I will be integrated $2\Delta t_c / \Delta t_b$ steps. The Euler backward scheme is used to the first integration of Mode–I then the leapfrog scheme is used. Note that the integration of Mode–I produces intermediate results of U and V at the $(n_c + 1)\Delta t_c$ time level, which are named $\tilde{U}$ and $\tilde{V}$ respectively and will be used in Mode–II.

(2) Mode–II: advection and dissipation process. The prognostic equations are

$$[U]^{n_c+1} = \tilde{U} + 2\Delta t_c \{ [-M(U)]^{n_c} + [D_u]^{n_c-1} \} \ , \tag{64}$$

$$[U]^{n_c+1} = \tilde{V} + 2\Delta t_c \{ [-M(V)]^{n_c} + [D_v]^{n_c-1} \} \ . \tag{65}$$

Note that the Asselin temporal filter is applied to both U and V at the $n_c\Delta t_c$ time level, i.e.,

$$[\mu]^{n_c} = \alpha_t [\mu]^{n_c} + (1-\alpha_t)([\mu]^{n_c+1} + [\mu]^{n_c-1}) \ , \tag{66}$$

where μ represents U or V, and α_t is the temporal filter coefficient.

(3) Mode–III: thermodynamic process. The prognostic equations for potential temperature and salinity are

$$[p_{bt}T]^{n_t+1} = [p_{bt}T]^{n_t-1} + 2\Delta t_t \{ -[\mathcal{L}(p_{bt}T)]^{n_t} + [p_{bt}\mathcal{Q}_T]^{n_t-1} \} \ , \tag{67}$$

$$[p_{bt} S]^{n_t + 1} = [p_{bt} S]^{n_t - 1} + 2\Delta t_t \{ - [\mathcal{L}(p_{bt} S)]^{n_t} + [p_{bt} \mathcal{Q}_S]^{n_t - 1} \} , \qquad (68)$$

where Δt_t represents the time step for tracers. The integrations of Mode–III may be asynchronous with Mode–II, if accelerating time step is used (Bryan, 1984).

Note that the horizontal velocity for tracers' advection is taken from the time–averaged velocity of Mode–I. Thus, if Δt_t is equal to Δt_c, Eqs.(67) and (68) are consistent with the bottom pressure tendency equation. In other word, if we set T or S equal to 1, the tracer equations will be exactly the same as the bottom pressure tendency equation. However, if the accelerating time step is used (i.e., $\Delta t_t \geqslant \Delta t_c$), the tracer equations in the flux form can lead to computational errors; thus, we will use the following form during the spin–up phase

$$\mu^{n_t + 1} = \mu^{n_t - 1} + 2\frac{\Delta t_t}{p_{bt}^{n_t}} \left\{ - \overline{\frac{\sqrt{p_{bt}}\, U}{a\cos\theta}}^{n_t} \frac{\partial T^{n_t}}{\partial \lambda} - \overline{\frac{\sqrt{p_{bt}}\, V}{a}}^{n_t} \frac{\partial T^{n_t}}{\partial \theta} \right.$$
$$\left. - \overline{p_{bt} \dot{\sigma}}^{n_t} \frac{\partial T^{n_t}}{\partial \sigma} + [p_{bt} \mathcal{Q}_T]^{n_t - 1} \right\} , \qquad (69)$$

where μ represents the tracers.

4. Experiment with idealized forcing of evaporation and precipitation

As a test for the model's ability to simulate thermohaline circulation in the oceans, we carried out an experiment in which the model ocean is driven by specified evaporation and precipitation. This experiment can help us to see whether the model can reproduce the theoretical solution of the Goldsbrough–Stommel circulation driven by evaporation and precipitation. A similar simulation of the three–dimensional circulation driven by evaporation minus precipitation was discussed by Huang (1993). In his model the natural boundary condition for salinity is applied to a modified version of the Bryan–Cox model, which is a z–coordinate model based on the rigid–lid approximation.

Our model basin is configured as a simple flat–bottom box extending 60° in longitude and from the equator to 60°N. The horizontal resolution is 4° × 3° in zonal and meridional directions. There are 15 σ layers vertically with thicknesses 0.0044, 0.0071, 0.0123, 0199, 0.0296, 0.0408, 0.0532, 0.0662, 0.0793, 0.0918, 0.1034, 0.1134, 0.1214, 0.1271, and 0.1302, gradually increasing downward.

In a close comparison with Huang (1993), we chose the same parameters: the horizontal viscosity and diffusivity are $A_m = 1 \times 10^9$ cm^2 s^{-1} and $\kappa_h = 1 \times 10^7$ cm^2 s^{-1} the vertical viscosity and diffusivity are $A_v = \kappa_v = 1$ cm^2 s^{-1}. We also assume simple linear (weighted by the cosine of the latitude) profile of evaporation minus precipitation

$$F_{E-P} = \frac{W_0}{\cos\theta} \left(1 - \frac{2\theta}{\theta_N} \right) , \qquad (70)$$

where $W_0 = 1$ m yr^{-1} is the amplitude of evaporation, θ_N is the northern boundary. Note that the net freshwater flux is zero within the whole basin.

The model is spun up from an initially homogeneous state of rest with a uniform salinity of 35 psu and temperature of 12.5°C. Since the pressure and density distributions for the given temperature and salinity fields are unknown, the model is first initiated to find the corresponding pressure and density distributions for a 5600 m–deep model ocean. The spun–up experiment went very smoothly, indicating that our numerical schemes are quite stable.
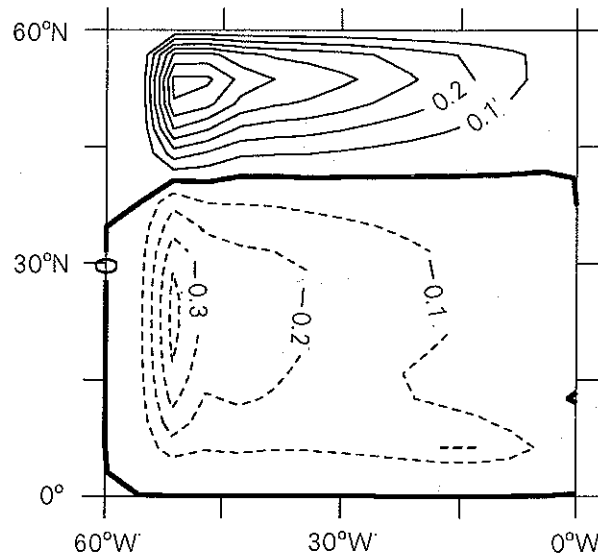
Fig. 1. The Goldsbrough–Stommel circulation driven by evaporation minus precipitation.

After 700 years integration the model is very close to a quasi–equilibrium state, and at the end of 5000–year integration, the model reached a steady state.

The model is capable of reproducing the barotropic Goldsbrough–Stommel gyres, as shown in Fig. 1. There is an anticyclonic barotropic gyre in the northern basin, driven by the precipitation, with a maximum streamfunction of about 0.7 Sv. Correspondingly, a cyclonic gyre appears south of 37°N with the maximum value of 0.4 Sv, about 0.1 Sv larger than that of Huang (1993).
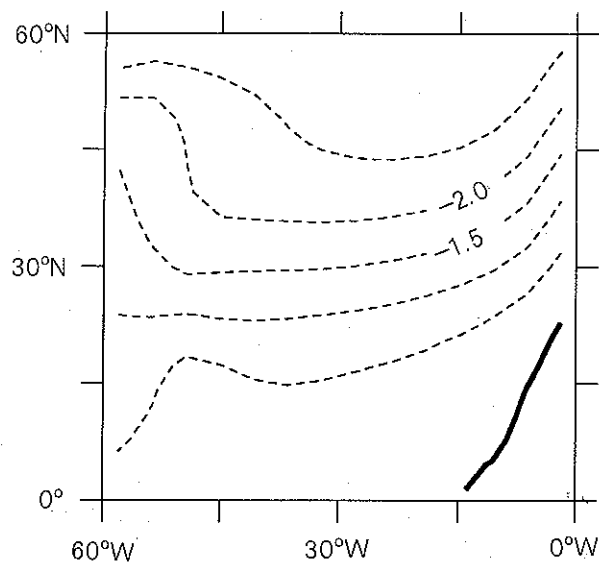
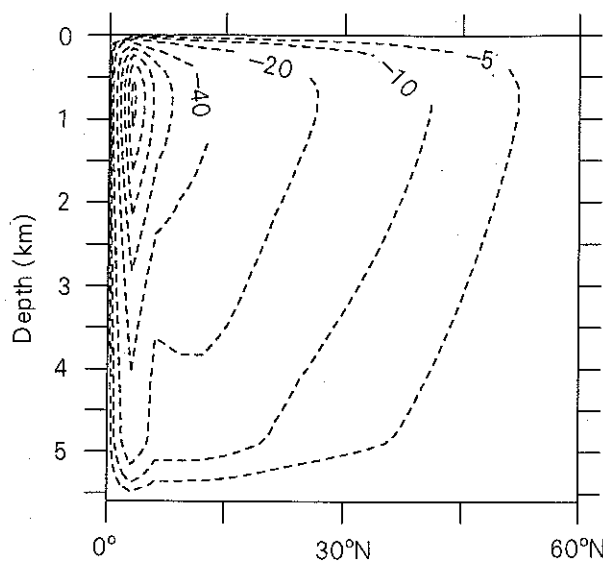Fig. 2. Surface salinity anomaly obtained from PCOM, units are in psu.

Fig. 3. Meridional overturning streamfunction, obtained from PCOM, units are in Sv.

The sea surface salinity anomaly (deviation from 35 psu) is also reproduced well (Fig. 2). A small positive salinity anomaly appears in the southeastern corner where the saline bottom water is formed. Except for the narrow regime of bottom water formation the surface salinity anomaly is negative everywhere, which indicates a halocline developed within the rest of upper ocean. The amplitude of the surface salinity is consistent with the scaling analysis suggested by Huang and Chou (1994).

The meridional overturning cell is in a haline mode with sinking near the southeastern corner and basin—wide upwelling (Fig. 3). Because the Coriolis forcing is quite weak within the region of deepwater formation, a small zonal pressure gradient can support a strong meridional current and lead to a strong meridional overturning cell at low latitudes. The maximum meridional overturning rate reaches 120 Sv, slightly larger than that reported by Huang (1993).

In conclusion, our new model has successfully reproduced the thermohaline circulation driven by evaporation and precipitation. The numerical results are consistent with the theoretical Goldsbrough—Stommel circulation and the previous numerical results obtained from a z—coordinate model based on the rigid—lid approximation.

5. Comparison with an equivalent Boussinesq model

5.1 *Equilibrium state*

In this section, we will compare the modeled equilibrium states obtained from PCOM and an equivalent free—surface model based on the Boussinesq approximations. For the sake of convenience, we name the latter the Boussinesq Compromised Ocean Model (BCOM hereafter). In order to make the model comparison as close as possible, these two models are based on almost exactly the same equations and finite difference schemes, except for several changes. Note that although these changes seem minor, their impact on the model's ability to

simulate the oceanic general circulation might be substantial, as will be shown in this study.

The BCOM is represented by a modified PCOM code in which several switches are turned on: (1) Reset $p_{b_t} = \bar{\rho}gh$, where $\bar{\rho}$ is a constant, $h = h_0(\lambda,\theta) + \eta(\lambda,\theta)$ is the total thickness of the ocean, η is the free surface. Thus, the bottom pressure tendency equation is now switched to an "almost" equivalent equation for the free surface elevation. Furthermore, the mass conservation in PCOM is now turned into a volume conservation in BCOM. (2) Replace density ρ by $\bar{\rho}$ in the momentum equations and diffusion terms. (3) Adopt a fixed pressure in each grid for the calculation of density, i.e., $\rho = \rho[T,S,p_0(\lambda,\theta,\sigma)]$, where pressure p_0 is set to the initial pressure at each grid and thus the pressure perturbations due to dynamic processes are excluded a priori.

Note that BCOM is a model based on σ coordinates. For the present case with no bottom topography, it is very close to a z–coordinate model. Note that BCOM is similar to many existing oceanic general circulation models based on the Boussinesq approximations, such as the free–surface modification of the Bryan–Cox model by Killworth et al. (1991), the σ–coordinate model by Blumberg and Mellor (1987), and the η–coordinate model developed at LASG (Zhang et al., 1996).

In our experiments, both PCOM and BCOM are forced with the same wind stress and thermohaline boundary conditions on the upper surface, including: the annual–mean global–zonal–averaged wind stress (Hellerman and Rosenstein, 1983); a linear profile of sea level atmospheric temperature $T_a = 25(1 - \dfrac{\theta}{\theta_N})$ °C; and a linear (weighted by the cosine of the latitude) profile of evaporation minus precipitation given by Eq.70 with $W_0 = 0.5$ m yr^{-1}. The horizontal resolution and sub–grid mixing / dissipation parameters are the same as those used in the previous freshwater–flux experiment, except for $\kappa_v = 0.3$ cm^2 s^{-1}, a value that is now commonly used in the numerical experiments of thermohaline circulation.

With the above prescribed forcing at the sea surface, the two models are spun up to a quasi–equilibrium from the initial rest and homogeneous states with temperature of 6°C and
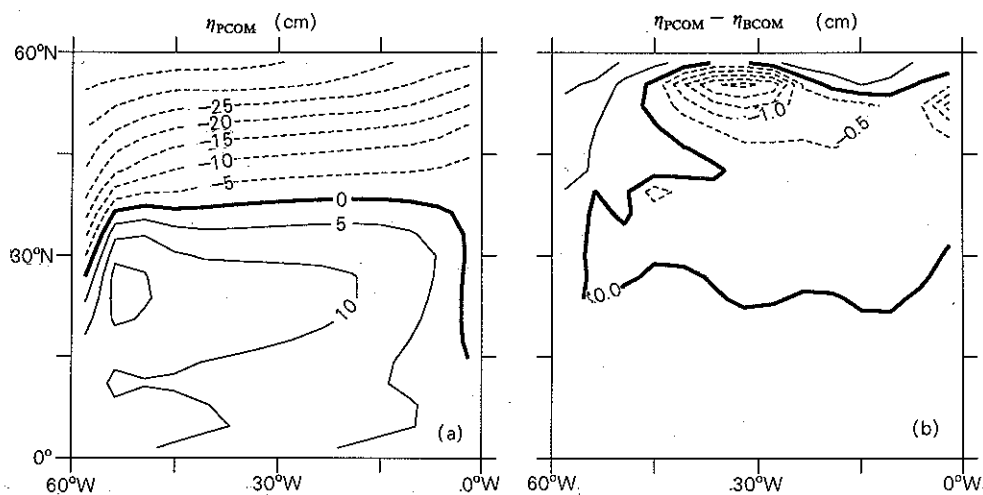

Fig. 4. The quasi–equilibrium states obtained from PCOM and BCOM, in cm. (a) sea surface elevation, subtracting the basin mean, obtained from PCOM; (b) the difference in sea surface elevation obtained from BCOM and PCOM.

salinity of 35 psu. The sea surface elevation and the difference obtained from these two models are shown in Fig. 4. Note that during the spin—up process there is a basin—wide decline of sea surface elevation in the PCOM due to cooling of the deep water. At the end of the 5000—year integration, the basin mean sea level in PCOM is 2.01 m below the initial level. On the other hand, the basin mean sea surface elevation in BCOM remains unchanged because the model conserves the total volume rather than the total mass. The sea surface elevation produced by PCOM, after subtracting the basin mean surface decline, is shown in Fig. 4a. A sea surface elevation maximum appears near the western edge of the subtropical basin where both the wind—driven circulation and the surface thermal forcing contribute to the formation of the sea surface elevation maximum. There is a general decline of the sea surface elevation toward high latitudes where the surface cooling leads to dense water and thus lower sea surface elevation. Subtracting this 2.01 m drop in the basin mean sea surface elevation, the difference in sea surface elevation between the two models is relatively small, but notable, (Fig. 4b). The largest difference is near the northern boundary. At the middle of the northern boundary where the sea level in PCOM is about 2.5 cm lower than that obtained from BCOM, and at the northwestern corner sea level in PCOM is 1.5 cm higher than in BCOM. Such errors in the free surface elevation is not negligible.

In general, at the quasi—equilibrium state with relatively low resolution, the temperature, salinity, and current distribution obtained from these two models are similar. It seems that in terms of simulation of the equilibrium state, the errors induced by the Boussinesq approximations are small in general. However, these two types of model may give rise to noticeably different solutions in some local regions, and we speculate that the difference in these special dynamic regions will increase as the model's horizontal resolution increases. More importantly, as we will discuss in the following section, these two models may behave quite differently during the transition from one state to another.

5.2 *Adjustment process*

As mentioned in the introduction, the essential difference between the two types of models is that the Boussinesq model replaces the mass conservation with volume conservation, and thus not only violates mass conservation but also distorts the energy conservation law. In the Boussinesq model, any diabatic process will lead to faulty mass sources / sinks, and give rise to a faulty pressure gradient force. In a rotating system, these faulty pressure signals induce some artificial adjustment processes. As a result, the pathway and final state of adjustment to the thermohaline perturbation can be quite different from those obtained from a truly compressible model.

As an example, we present results from two parallel numerical experiments based on PCOM and BCOM. Both models were restarted from their quasi—equilibrium states described in the previous section. For the first 10 years, we imposed an anomalous surface heat flux of 20 W m^{-2} over the latitude band between 45°N and 57°N. The heat flux anomaly was withdrawn at the end of year 10. The thermal boundary condition on the sea surface is the following equation regulating the heat flux through the air—sea interface

$$F_\mathrm{H} = K(T_a - \overline{T}_o) + K(\Delta T_a - \Delta T_o) + \Delta F(\theta, t) , \tag{71}$$

where $K = 40$ W m^{-2} K^{-1}; $\overline{T}_o$ represents the the model's climatological sea surface temperature; $\Delta T_o = T_o - \overline{T}_o$ is the sea surface temperature anomaly; ΔF is the imposed heat flux anomaly; ΔT_a is the change in atmosphere temperature, which is determined by using a 0—dimension energy balance atmospheric model. If one neglects the heat capacity of the

atmosphere, the perturbation form of the energy balance equation may be expressed as

$$0 = - K_r \Delta T_a + K(\Delta T_o - \Delta T_a) , \tag{72}$$

where $K_r = 2.4$ W m^{-2} K^{-1} is the atmospheric radiative feedback constant. Thus, ΔT_a can be solved as a function of ΔT_o . The final form for the surface heat flux is

$$F_H = \frac{KK}{K + K_r} (T_a - \overline{T}_o) + \frac{KK_r}{K + K_r} (T_a - T_o) + \Delta F(\theta, t) . \tag{73}$$

Therefore, the thermal boundary condition used here is slightly different from that used in the spin—up experiment. In the previous case the sea surface atmospheric temperature T_a is fixed (this is equivalent to assuming an infinite heat capacity of the atmosphere); in the adjustment experiments the sea surface atmospheric temperature is no longer fixed, instead the new atmospheric temperature $T_a + \Delta T_a$ will change in response to the changed sea surface water temperature. The strong feedback guarantees that the difference in the air—sea temperature remains relatively small. This boundary condition is actually equivalent to coupling the oceanic model with an energy balance model for the atmosphere (Zhang et al., 1993). The application of this modified thermal boundary condition puts a constraint on the air—sea heat flux. In particular, it prevents excessive air—sea heat flux to appear in the process of rapid cooling / heating.

    The time evolution of the thermohaline circulation in these two models went through rather different paths. With the heating anomaly in the region of deepwater formation, the modeled thermohaline circulations in the two models went through a similar weakening phase during the first 10 years. The maximum meridional overturning rate declined continuously from 15.1 Sv to 4.5 Sv in PCOM, while it declined from 16.0 Sv to 5.7 Sv in BCOM. Note that the quasi—equilibrium states in these two models are slightly different. The initial unperturbed meridional overturning rate in BCOM is about 0.9 Sv larger than that in PCOM. In order to compare the meridional circulation in these two models, we plot the time evolution of the
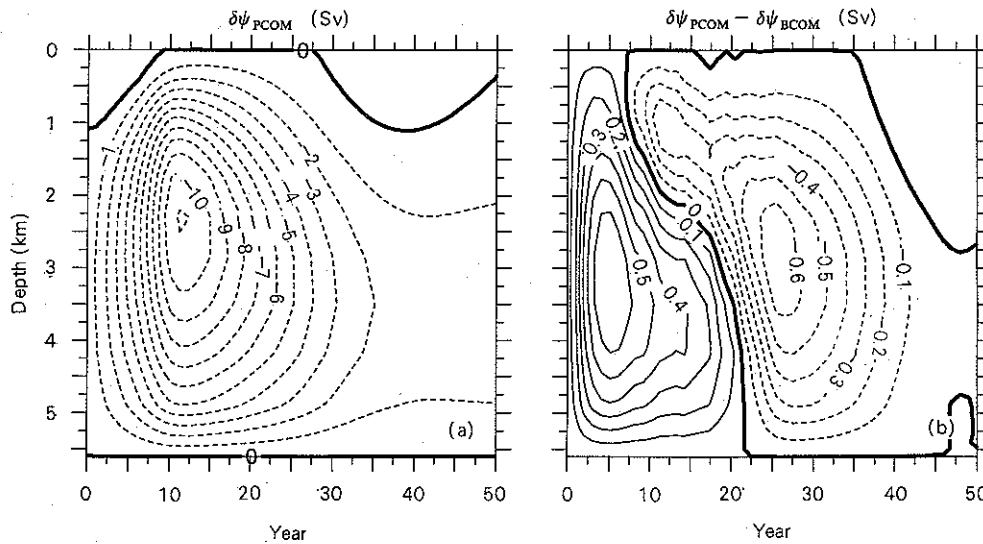

Fig. 5. (a) Time evolution of the anomaly of meridional overturning streamfunction along the vertical section at 54°N in PCOM; (b) the difference of the anomaly between PCOM and BCOM.

mereidional streamfunction at a section at 54°N, denoting as δM^*. Compared with PCOM, the thermohaline circulation in BCOM declined too fast in the beginning, so $\delta M^*_{\text{PCOM}} - \delta M^*_{\text{BCOM}}$ is positive (Fig. 5b). The largest error is about 0.6 Sv. If we define the relative error at any given time as $\varepsilon = \dfrac{M^*_{\text{PCOM}} - M^*_{\text{BCOM}}}{M^*_{\text{PCOM}}}$, the maximum error is about 20% during the first five years.

At the end of year 10 the heat flux anomaly ΔF was reset to zero, and the thermohaline circulation started to recover, with slight delay due to the inertia of the system. For example, at 54°N, the meridional overturning rate in PCOM kept declining for another two years before it started to recover (Fig. 5a).

The difference in the anomalous meridional streamfunciton became negative after year 20, reached a local minimum at year 25, and recovered afterward. The negative value of this difference indicates that the recovery of the thermohaline circulation at this section in BCOM is faster than in PCOM for the time beyond year 20.

In previous studies, such as those of Greatbatch (1994), Mellor and Ezer (1995), Dukowicz (1997), many investigators have concluded that the Boussinesq models can predict sea level changes with acceptable accuracy by including a global uniform, time–dependent correction term. We emphasize that the adjustment processes in response to heating may be different in these two types of model. In PCOM sea level increases as a direct response to the local heating; there is no bottom pressure perturbation initially, so the adjustment processes are baroclinic in nature. On the other hand, heating induces a loss of mass locally in BCOM. As a result, there is a negative bottom pressure anomaly, which will induce a global adjustment of mass. Such adjustment is barotropic in nature. Due to this faulty source of mass, the pressure perturbations and the associated velocity perturbations during the adjustment processes may be quite different from that in the real oceans.

In fact, we have produced preliminary results that indicated noticeable errors in the simulation of sea surface height anomaly in BCOM. For example, at the year 10, sea surface elevation along the northern boundary raised up to 11 cm in PCOM. On the other hand, the change in sea surface elevation was underestimated about 1.1 cm in BCOM (Fig. 6). The relative errors is about 10%. Note that the sea level elevation anomaly in BCOM has been corrected by a globally uniform, time–dependent factor calculated from the volume–averaged density change (Greatbatch, 1994). Assuming the global–integrated evaporation minus precipitation rate is zero, the global–mean bottom pressure correction is

$$\overline{\delta p_b} = \frac{1}{A} \iint_A \delta p_b \, dx dy \ ,$$

where A is the total area of the model ocean, and $\delta p_b = p_b - p_b^0$ is the bottom pressure deviation from the initial value p_b^0. The free surface elevation, including the correction, for BCOM is

$$\delta \eta^* = \delta \eta - \frac{1}{\rho_0 g} \overline{\delta p_b} \ .$$

Note that the simple correction term defined in the equation above does not guarantee that the basin–mean sea surface elevation in BCOM will match that in PCOM. As shown in Fig. 7a, due to the global warming up of the model basin under the heating anomaly, the basin–mean sea surface height anomaly in PCOM is larger than that in BCOM (including the
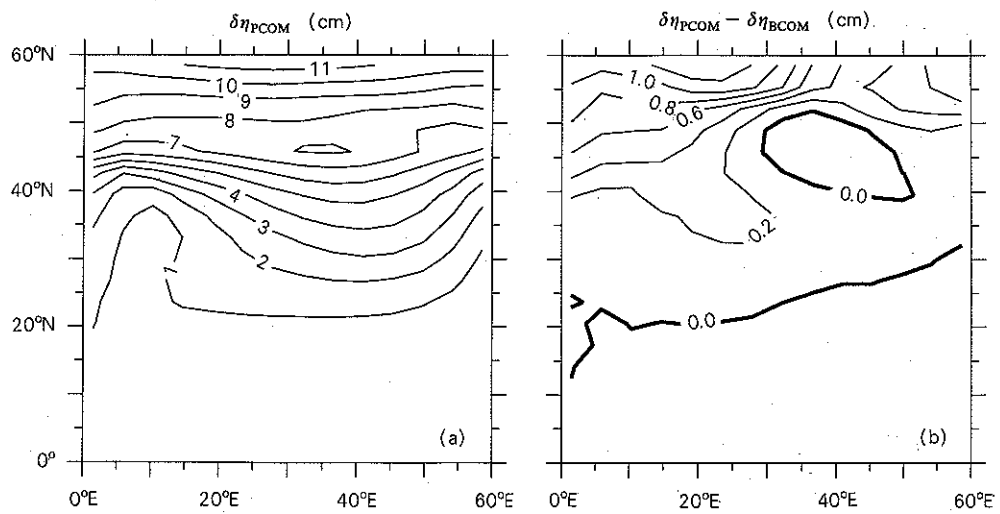
Fig. 6. (a) Annual mean sea level elevation anomaly in PCOM at the year 10; (b) the difference between PCOM and BCOM.
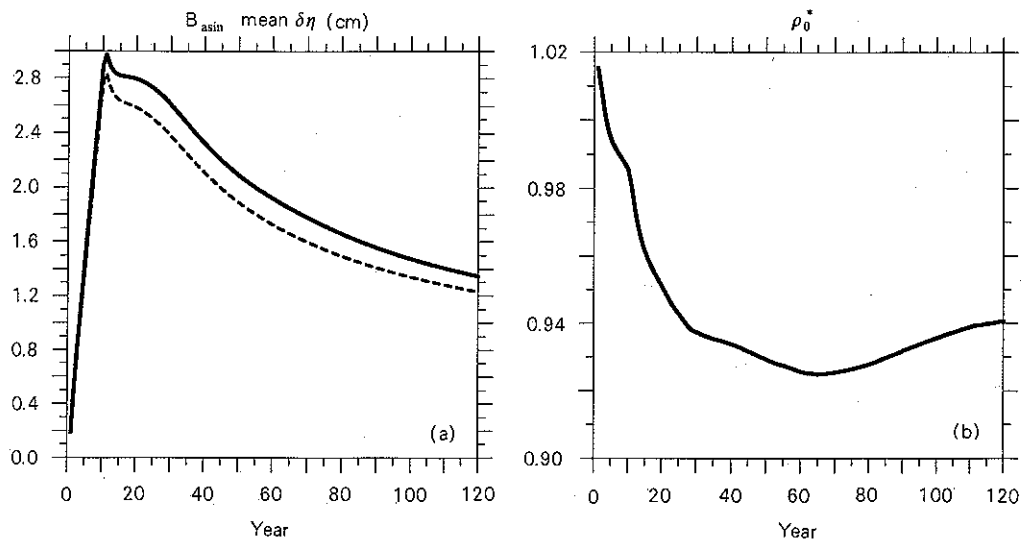

Fig. 7. (a) the basin mean sea surface height anomaly induced by the heating source imposed along the northern boundary, the solid line for PCOM and the dashed line for BCOM (with the global correction). (b) The suitable mean density required for a perfect match between BCOM and PCOM.

global correction term). To make a perfect match one needs an equivalent mean density that can deliver the right amount of sea surface elevation change

$$\rho_0^* = -\frac{\overline{g\eta_{\text{pcom}}}}{\delta p_b} \ .$$

As shown in Fig. 7b, the equivalent mean density that yields the correct basin—mean sea surface height anomaly actually varies with time. For the case of heating anomaly, this ρ_0^* is actually less than one for the most time. Without a "correct model", such as PCOM, one is, of course, unable to calculate this ρ_0^*; thus, a truthfully global correction is impossible for models based on Boussinesq approximations.

Assuming the mean density of $\rho_0 = 1.029$, the time evolution of the sea surface elevation indicated a coherent 10% difference between the two models (Fig. 8). As discussed above, the spatially uniform correction may not always yield the right solutions when the scale of the perturbations is comparable with the barotropic radius of deformation. As discussed above, the simple correction term does not guarantee that the basin—mean sea surface elevation in BCOM would match that in PCOM. Because the ρ_0 used to calculate the global correction is larger than the suitable mean density displayed in Fig. 7b, the global mean sea surface height anomaly in BCOM (with correction) is smaller than that in PCOM. In fact, the difference between PCOM and BCOM is positive along both the northern and southern boundaries, in contrast to Fig. 4b where the difference in the steady state has a zero basin—mean.

We have shown that the time evolution and the adjustment in response to thermal forcing can be quite different in PCOM and BCOM. These differences are due to the errors introduced through the Boussinesq approximations. In particular, the faulty sources of mass associated with heating / cooling may be the major source of errors in BCOM. The details of the adjustment and the dynamic processes lead to such differences are, however, very complicated. In order to understand these processes, one can apply the theory of geostrophic adjustment by studying the response to the initial thermal forcing (or mixing) in terms of an initial pressure perturbation and tracing the adjustment processes hereafter. This can be done by following some of the classic theory of geostrophic adjustment. For example, Rossby
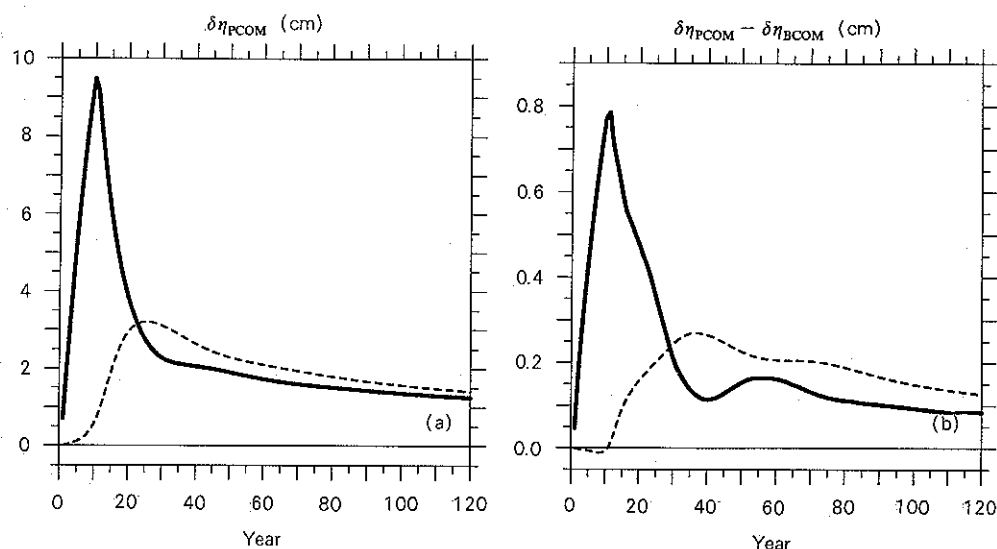

Fig. 8. Sea surface elevation anomaly calculated from (a) PCOM and (b) PCOM—BCOM. Thin solid lines indicate the anomaly averaged over a zonal band near the northern boundary, 48—60°N; the dashed lines indicate that for the southern boundary, and the heavy lines are the difference between northern and southern boundaries 0—15°N.

(1938) first studied the mutual adjustment of velocity and pressure fields. However, Yeh (1957) pointed out that the direction of this mutual adjustment depends on the horizontal scale of the initial perturbation fields. Thus, the results of the adjustment of the system in response to thermal forcing in PCOM and BCOM depend on the horizontal scale of the initial thermohaline perturbations; however, the detailed analysis is beyond the scope of this paper. We are currently in the process of analyzing the data generated through these numerical experiments, and the results will be reported in subsequent paper.

6. Conclusions

We have developed an oceanic general circulation model based on pressure coordinates. In departure from the commonly used oceanic circulation models, our new model avoids the Boussinesq approximations. The major features of the new model include: 1) using the exact form of mass conservation, 2) using the in–situ instantaneous pressure and the UNESCO equation of state to calculate density, 3) using the in–situ density in the momentum equations, 4) using finite difference schemes that conserve total energy.

The model has been tested for many standard cases of wind–driven and thermohaline circulation. Our preliminary tests demonstrated that the model runs smoothly and produces results that are similar to those obtained from BCOM, an equivalent model based on the Boussinesq approximations. However, our numerical experiments also indicate that even for the quasi–equilibrium state obtained for relatively low resolution, the free surface elevation and bottom pressure produced from our model can be somewhat different from that produced by BCOM.

Most importantly, using PCOM or BCOM to simulate the time evolution of the circulation under anomalous thermal forcing can lead to noticeable difference. These differences are due to the approximations used in BCOM. Especially, there are faulty mass sources due to the no–divergence approximation, which can give rise to much distorted dynamic processes during the adjustment period. These processes are complex and they cause some major differences in the system, so further study is needed to examine the details.

A specific feature of this new model is that the bottom pressure is a prognostic variable, so the bottom pressure data obtained from the new high–accuracy gravity satellite mission can be assimilated into the model, thus substantially improving the model's ability to simulate the oceanic circulation. On the other hand, although bottom pressure can be diagnosed in the Boussinesq models, the sign of the bottom pressure might be wrong, and the time evolution of the bottom pressure in such models is distorted, primarily due to the faulty source of mass.

More than 30 years ago, when ocean modelers were forced to use half precision in their calculations in order to save computer memory, so many approximations were both convenient and technically necessary. With the rapid advance of computer technology, we strongly believe that it is the right time that we should study the oceanic circulation without the possible compromise associated with some unnecessary approximations. In fact, the PCOM is run with double precision, so that the density calculated is consistent with the UNESCO subroutine. Using pressure coordinates and abandoning the Boussinesq approximations are just a step in this direction.

REFERENCES

Asselin, R. 1972: Frequency filter for time integrations. *Mon. Wea. Rev.*, **100(6)**, 487–490.

Blumberg, A. F., and J. Mellor, 1987: A description of a three–dimensional coastal ocean circulation model. In *Three–dimensional Coastal Ocean Models*, Vol. 4, N. Heaps, Ed., Am. Geophys. Union, 208 pp.

Boussinesq, J., 1903: Theorie analyque de la chaleur (Paris: Gathier–Villars), Vol. 2.

Bryan, K., 1969: A numerical method for the study of the circulation of the world ocean. *J. Comput. Phys.*, **4**, 347–376.

Bryan, K., 1984: Accelerating the convergence to equilibrium of ocean–climate models. *J. Phys. Oceanogr.* **14**, 666–673.

Dewar, W. K., Y. Hsueh, T. J. McDougall, and D. Yuan, 1998: Calculation of pressure in ocean model simulations. *J. Phys. Oceanogr.*, **28**, 577–588.

Dukowicz, J. K., 1997: Steric sea level in the Los Alamos POP code–non–Boussinesq effects. In *Numerical methods in atmospheric and oceanic modeling, the Andre Robert memorial volume* (C. Lin, R. Laprise, H. Richie, Eds.), Canadian Meteor. Oceanogr. Soc., Ottawa, Canada, 534–546.

Greatbatch, R. J., 1994: A note on the representation of steric sea level in models that conserve volume rather than mass. *J. Geophys. Res.*, **99**, 12767–12771.

Hellerman, S. and M. Rosenstein, 1983: Normal monthly wind stress over the world ocean with error estimates. *J. Phys. Oceanogr.*, **13**, 1093–1104.

Huang, R. X., 1993: Real freshwater flux as a natural boundary condition for the salinity balance and thermohaline circulation forced by evaporation and precipitation. *J. Phys. Oceanogr.*, **23**, 2428–2446.

Huang, R. X., and R. Chou, 1994: Parameter sensitivity study of the saline circulation. *Clim. Dyn.*, **9**, 391–409.

Jackett, D. R., and T. J. McDougall, 1995: Stabilization of hydrographic data. *J. Atmos. Ocean. Tech.*, **12**, 381–389.

Killworth, P., D. D. Stainforth, D. J. Webb, and S. M. Paterson, 1991: The development of a free–surface Bryan–Cox–Semtner ocean model. *J. Phys. Oceanogr.*, **21**, 1333–1348.

Mellor, G. L., and T. Ezer, 1995: Sea level variations induced by heating and cooling: an evaluation of the Boussinesq approximation in ocean models. *J. Geophys. Res.*, **100**, 20, 565–20, 577.

Mihalian, J. M., 1962: A rigorous derivation of the Boussinesq approximation applicable to a thin layer of fluid. *Astrophys. J.*, **136**, 1126–1133.

Rossby, C. G., 1938: On the mutual adjustment of pressure and velocity distributions in certain simple current systems, II. *J. Mar. Res.*, **1**, 239–263.

Spiegel, E. A., and G. Veronis, 1960: On the Boussinesq approximation for a compressible fluid. *Astrophys. J.*, **131**, 442–447.

Yeh, T. C., 1957: On the formation of quasi–geostrophic motion in the atmosphere. *J. Meteor. Soc. Japan*, the 75th Anniversary Volume, 130–134.

Zeng, Q. C., and X. H. Zhang, 1982: Perfectly energy–conservative time–space finite–difference schemes and the consistent split method to solve the dynamical equations of compressible fluid. *Scientia Sinica* (Series B), **25(8)**, 866–880.

Zeng, Q. C., and X. H. Zhang, 1987: Available energy conserving schemes for primitive equations on spherical baroclinic atmosphere. *Scientia Atmopsheric Sinica*, **11(2)**, 113–127 (in Chinese).

Zeytounian, R. K., 1989: The Benard problem for deep convection: rigorous derivation of approximate motions. *Int. J. Eng. Sci.*, **27**, 1361–1366.

Zhang, S., R. J. Greatbatch, and C. A. Lin, 1993: A reexamination of the polar halocline catastrophe and implications for coupled ocean–atmopshere modeling. *J. Phys. Oceangy.*, **23**, 287–299.

Zhang, X. H., K. Chen, X. Jin, W. Lin, and Y. Yu, 1996: Simulation of thermohaline circulation with a twenty–laye oceanic general circulation model. *Theor. Appl. Climatol.*, **55**, No.1–4, 65–87.

UNESCO, Tech. Papers in Marine Sci., No.36. Paris, 1981.

一个压力坐标下的海洋环流模式

黄瑞新   金向泽   张学洪

摘 要

作者们构造了一个新的、压力(p)坐标下海洋环流模式。由于海底压力是随时间变化的，所用的垂直坐标实际上是 p—sigma 坐标。模式的数值解满足一套能量守恒的有限差分格式。模式的最重要的新特点在于它是一个完全可压缩的海洋模式，没有采用 Boussinesq 近似。新模式在以下几方面不同于现有的许多模式：1)精确的质量守恒形式；2)计算密度时使用的是现场的瞬时压力和 UNESCO 的状态方程；3)动量方程的密度也使用现场密度；4)保持总能量守恒的差分格式。初始的试验表明模式程序运行顺畅且非常稳定。新模式模拟的准稳态环流型同现有模式是一致的，不过达到这种准稳态环流型的时间演变过程则很不一样。这种非 Boussinesq 模式可以为气候研究和卫星观测提供更加精确的信息。

关键词：非 Boussinesq, 压力坐标, 质量守恒模式